

Wednesday 25 Nov

Plasma FIB-SEM for multi-modal materials characterization

Free webinar

16.15-17.15 CET | 10.15-11.15 EST

[Register here](#)



Dean Miller
Senior Scientist,
Tescan

Wiley Analytical Science



Nanometric Chemical Analysis of Beam-Sensitive Materials: A Case Study of STEM-EDX on Perovskite Solar Cells

Felix Utama Kosasih, Stefania Cacovich, Giorgio Divitini, and Caterina Ducati*

Quantitative chemical analysis on the nanoscale provides valuable information on materials and devices which can be used to guide further improvements to their performance. In particular, emerging families of technologically relevant composite materials such as organic–inorganic hybrid halide perovskites and metal-organic frameworks stand to benefit greatly from such characterization. However, these nanocomposites are also vulnerable to damage induced by analytical probes such as electron, X-ray, or neutron beams. Here the effect of electrons on a model hybrid halide perovskite is investigated, focusing on the acquisition parameters appropriate for energy-dispersive X-ray spectroscopy in a scanning transmission electron microscope (STEM-EDX). The acquisition parameters are systematically varied to examine the relationship between electron dose, data quality, and beam damage. Five metrics are outlined to assess the quality of STEM-EDX data and severity of beam damage, further validated by dark field STEM imaging. Loss of iodine through vacancy creation is found to be the primary manifestation of electron beam damage in the perovskite specimen, and iodine content is seen to decrease exponentially with electron dose. This work demonstrates data acquisition and analysis strategies that can be used for studying electron beam damage and for achieving reliable quantification for a broad range of beam-sensitive materials.

Over the last decade, hybrid halide perovskite photovoltaic devices have experienced a rapid advance in efficiency and stability.^[1,2] An essential factor contributing to this success is the investigation of perovskite solar cells (PSCs) using a wide range of characterization techniques across multiple length scales, with a goal of relating PSCs' remarkable macroscopic optoelectronic properties to their micro- and nanoscale crystal structure and chemical composition.^[3,4] Due to the complex interplay of


multiple parameters and processes, such studies often require a combination of advanced methods. In particular, energy-dispersive X-ray spectroscopy (EDX) in a scanning transmission electron microscope (STEM) is a powerful and versatile tool that allows nanoscale investigation of many materials' morphology and elemental composition. Recent improvements in the technical capabilities of analytical STEMs, such as the development of windowless silicon drift detectors (SDDs), have ameliorated the two primary weaknesses of EDX: its low detection efficiency and inability to detect light elements.^[5] Additionally, post-processing data treatments based on multivariate statistical analysis can extract more detailed information from complex and noisy data, such as those generated in STEM-EDX analysis.^[6,7]

In principle, the reliability of quantitative EDX analysis is strongly dependent on signal/noise ratio across the energy spectrum, which in turn depends on the number of characteristic and bremsstrahlung X-rays emitted by the

sample and on the detector's collection efficiency. The latter is generally limited by the small solid angle accessible in a (S) TEM column (up to ≈ 0.9 sr in state-of-the-art designs) to 1–7% of the generated X-rays. The former, for a given specimen thickness, depends on the electron dose (number of probe electrons per unit area of specimen) and hence can be increased to obtain characteristic X-ray peaks which are quantifiable with higher accuracy by increasing either the beam current or the dwell time. It follows that for elements present in small concentrations, or those with lower X-ray generation rates, precise quantification would require high electron doses. However, this is very challenging when dealing with organic–inorganic nanocomposites, such as hybrid halide perovskites, as such materials are prone to beam damage when subjected to high-intensity electron bombardment.^[8–11] Previous research has shown that the primary beam damage mechanism for hybrid perovskites is radiolysis or ionization damage which causes bond breaking and disintegration of the perovskite crystal structure.^[12,13] Possible results of radiolysis include formation of vacancies through atomic/ionic displacement and loss of volatile molecules.^[14,15] Both types of damage affect the accuracy of elemental quantification in STEM-EDX, with the latter being more detrimental as it is usually accompanied by a transformation of the pristine specimen into another chemical phase. In

F. U. Kosasih, Dr. G. Divitini, Prof. C. Ducati
Department of Materials Science and Metallurgy
University of Cambridge
27 Charles Babbage Road, Cambridge CB3 0FS, UK
E-mail: cd251@cam.ac.uk

Dr. S. Cacovich
CNRS-IPVF
Institut Photovoltaïque d'Île-de-France
UMR 9006, 18, Boulevard Thomas Gobert, Palaiseau 91120, France

 The ORCID identification number(s) for the author(s) of this article can be found under <https://doi.org/10.1002/smt.202000835>.

© 2020 The Authors. Small Methods published by Wiley-VCH GmbH. This is an open access article under the terms of the Creative Commons Attribution License, which permits use, distribution and reproduction in any medium, provided the original work is properly cited.

DOI: 10.1002/smt.202000835

halide perovskites, it is well known that iodide diffuses easily due to its low migration activation energy, making iodine loss a likely manifestation of beam damage.^[16–18] Indeed, EDX conducted in TEM mode with a parallel electron beam and selected area electron diffraction (SAED) have been shown to cause decomposition of MAPbI₃ into hexagonal PbI₂ through formation of iodine vacancies and eventual loss of volatile gases.^[10,14]

Other than electron dose, an influential parameter in TEM characterization of beam sensitive materials is dose rate (dose per unit time). Low dose rates, achieved by using low beam currents or a broad parallel beam, are expected to cause minimal beam damage. On the other hand, STEM-EDX normally involves high dose rates, whose effect is not as clear due to the complex pathways and timescales of damage mechanisms in inorganic materials and the relatively long readout times of EDX detectors.^[19]

In this work, we outline and test several metrics to quantify STEM-EDX data quality and beam damage by systematically varying acquisition conditions on a well-studied PSC architecture. We use these robust metrics to estimate quantification errors and demonstrate spatial rebinning as a powerful method to reduce such errors. This study further shows that minimizing electron dose for the acquisition of STEM-EDX spectrum images (SIs) of hybrid halide perovskites is of utmost importance. Finally, we produce Pb, I, and Br elemental maps with minimized statistical uncertainty. The principles outlined herein can be extended to characterization of other soft and composite materials with high-energy probes.

An electron-transparent cross-sectional slice of a PSC, called a lamella, can be prepared with focused ion beam (FIB) milling (Note S1 and Figure S1, Supporting Information). In this work, we use a state-of-the-art triple-cation, double-halide (TCDH) perovskite with a nominal stoichiometry of Cs_{0.06}FA_{0.79}MA_{0.15}Pb(I_{0.85}Br_{0.15})₃. This composition, or slight variations thereof, is commonly used in highly efficient PSCs.^[20] The perovskite layer is sandwiched between a gold anode, spiro-OMeTAD (2,2',7,7'-tetrakis(N,N-di-p-methoxyphenyl-amine)9,9'-spirobifluorene) hole transport layer, TiO₂ electron transport layer, indium tin oxide cathode, and glass substrate (Figure S2a, Supporting Information).

We first explore the effect of electron dose on the quality of STEM-EDX data. We acquire 12 STEM-EDX SIs using combinations of 4 beam current and 3 dwell time values as detailed in Table 1. To reduce the possibility of cross-talk between adjacent pixels, we undersample the STEM-EDX scans using a spatial sampling of 10 nm per pixel (the probe diameter is calculated to be about 8 nm after taking beam broadening into account). We also acquire a pair of high-angle annular dark field (HAADF) images, one taken before and another after the STEM-EDX scans (Figure S2, Supporting Information). As the dwell time per pixel for HAADF imaging is 1 μs, and no change is detectable after single imaging scans, we infer that their contribution to specimen damage is negligible in comparison to STEM-EDX mapping.

STEM-EDX data quality for different electron doses must be determined to understand the quantification accuracy achievable while using minimum electron doses. In EDX, the background-corrected peak intensity for a characteristic X-ray line is assumed to be related to the number of atoms of the corresponding element present in the specimen. For

Table 1. Electron beam current parameters used to acquire 12 STEM-EDX SIs. The dose rates are calculated using a pixel size of 100 nm². All dose rate and dose values are rounded to the nearest 10.

Beam current [pA]	Dose rate [e ⁻ Å ⁻² s ⁻¹]	Dwell time [ms]	Dose [e ⁻ Å ⁻²]
64	39 950	10	400
		30	1200
		50	2000
107	66 780	10	670
		30	2010
		50	3340
155	96 740	10	970
		30	2910
		50	4840
242	151 050	10	1510
		30	4540
		50	7560

all dose values used in this work, the raw X-ray counts per energy channel is too low to perform further pixel-by-pixel analysis with statistical confidence. Therefore, we first spectrally rebin the SIs by a factor of four, reducing spectral resolution from 5 eV per channel to 20 eV per channel. Then, we work on the statistical ensemble of all pixels in each SI, performing principal component analysis (PCA) to denoise the data as described in our previous work.^[7] PCA finds linear combinations of variables (components) in the raw data which best explain the data's variance. These components are ranked based on their proportion of the raw data's overall variance, then we construct a denoised SI composed of only statistically significant components by excluding the low-variance noise components. From this denoised SI, we can extract peak intensity and background level data to evaluate chemical composition in the same way as we would from the raw EDX SI, except that now the data has a much higher signal/noise ratio. We refer readers to ref. [7] for a detailed explanation of PCA and its application in STEM-EDX.

The PCA-treated EDX data are first examined to check for peak detectability (PD) of the Pb-L_α, I-L_α, and Br-K_α peaks, the elemental lines of highest interest for TCDH perovskite. A peak is considered detectable at a 99% confidence interval (CI) if $I/\sqrt{B} \geq 3$, where I is the background-corrected peak intensity and B is the background level.^[21,22] Maps of PD at 99% CI are shown in Figure 1, where the red/blue shading indicates the difference between the measured I/\sqrt{B} and the critical value required to achieve PD. The I-L_α and Pb-L_α peaks are easily detectable even with the lowest dose, but for this specific perovskite formulation, the Br-K_α peak only becomes consistently detectable with a dose of 2910 e⁻ Å⁻² due to the relatively low bromine content compared to iodine or lead. One may use the slightly more intense Br-L_α peak instead, but the signal count increase is marginal (Figure S3, Supporting Information) and Br-L_α has a higher chance of overlapping with other peaks due to its much lower energy (Al-K_α being the most probable case for optoelectronic device specimens).

Once PD has been established, we choose two parameters to evaluate the quality of PCA-treated EDX data corresponding to the main characteristic peaks (Figure 2a,b). The first is relative error (RE) at a 95% CI, here taken as the error in the measurement of background-corrected peak intensity I at each pixel,

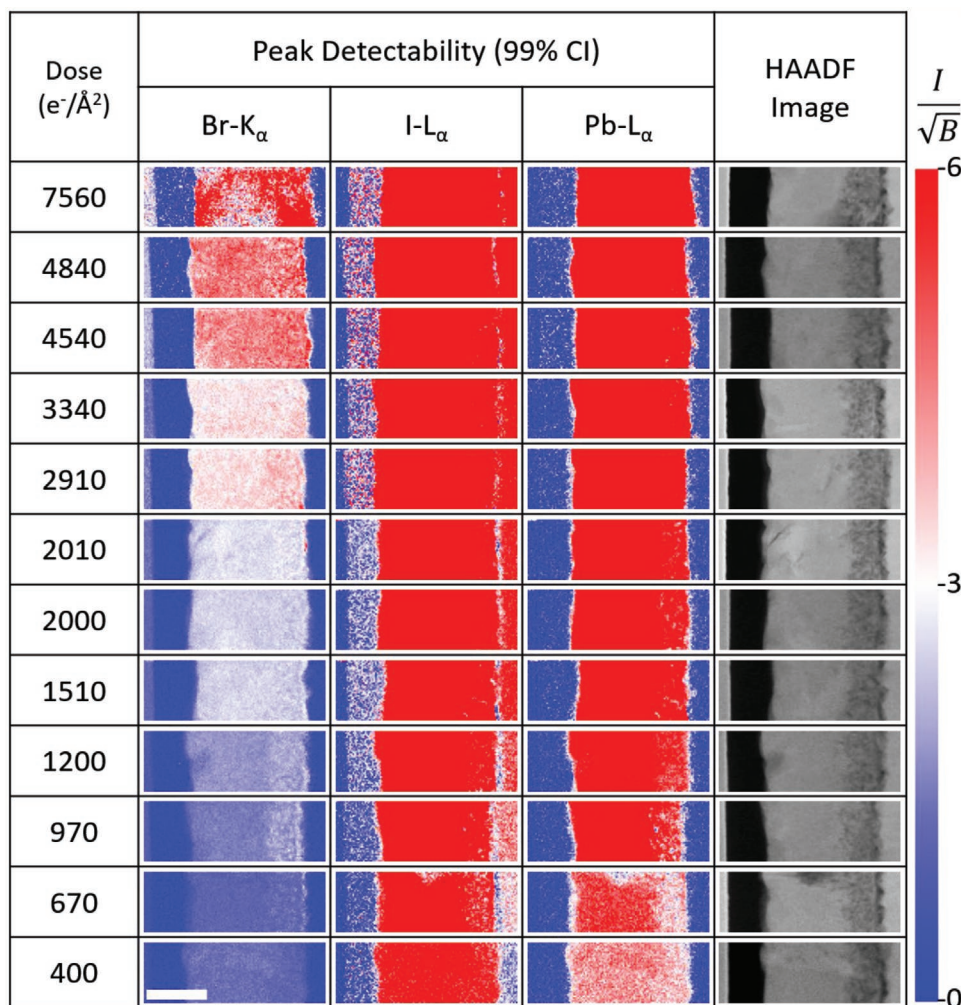


Figure 1. Maps of STEM-EDX peak detectability at a 99% CI and reference HAADF images acquired before STEM-EDX mapping. Red-shaded pixels are detectable while blue-shaded pixels are not. The red/blue shading indicates how far a pixel's I/\sqrt{B} metric is from the critical value (white) needed to achieve detectability. The maps' spatial resolution is 10 nm per pixel. Scale bar represents 0.4 μm and applies to all maps and images.

averaged across n pixels identified as a specific compound, in this case perovskite. As X-ray counts follow Gaussian statistics, RE can be calculated as^[21]

$$\text{RE} = \frac{100\%}{n} \sum_1^n \frac{1.96}{\sqrt{I}} \quad (1)$$

The RE (Figure 2a) remains high even at the highest dose, with values of 33%, 24%, and 74% for Pb, I, and Br, respectively. Because RE is proportional to $I^{-0.5}$, there is limited benefit in further increasing the electron dose as shown by the plateaus in Figure 2a. Although this high degree of error precludes accurate quantification, the data contains useful qualitative information on spatial heterogeneity. A more accurate assessment of composition can be made on a many-pixel basis by examining a large number of pixels contained in the SI. The appropriate error metric for this approach is no longer RE but absolute error (AE), which we choose as the second EDX data quality parameter. AE at a 95% CI, expressed as a percentage of the mean peak intensity (MPI),

is calculated according to Equation 2, where MPI (σ) is the mean (standard deviation) of background-corrected peak intensity calculated from n pixels of the chemical species of interest, in this case perovskite.

$$\text{AE} = \frac{1.96\sigma}{\sqrt{n}} \times \frac{100\%}{\text{MPI}} \quad (2)$$

In this experiment, n is ≈ 2080 for each SI, with slight variations (up to $\pm 6\%$) from one SI to another due to the roughness of the films. This high n results in low AE values of 0.5–1.6% of MPI across the dose range (Figure 2b). We note that the AE for Br- K_{α} is unexpectedly high for the highest electron dose. This is most likely due to the abnormally heterogeneous bromine distribution in the corresponding scan area (see Figure S4, Supporting Information) rather than the electron dose itself, as the AEs for Pb- L_{α} and I- L_{α} at this dose agree well with the trend established by previous data points. There are common acquisition conditions where n may be far lower or higher than 2080. At low magnification ($\approx 20\text{kX}$ or less) STEM-EDX scans of

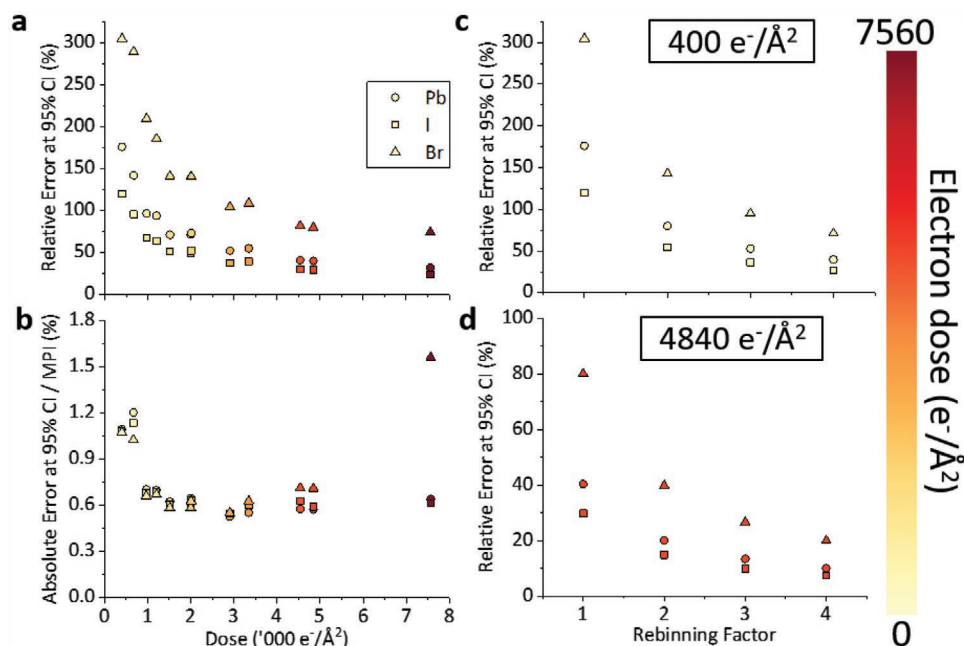


Figure 2. STEM-EDX measurement errors for Pb- L_{α} , I- L_{α} , and Br- K_{α} peaks across a range of electron doses and the effect of spatial rebinning on them. a) Relative error on an individual pixel basis at a 95% CI and b) absolute error for a whole SI at a 95% CI, expressed as a percentage of MPI. Effect of spatial rebinning on relative error for the SI acquired using a dose of c) $400 \text{ e}^{-} \text{ \AA}^{-2}$ and d) $4840 \text{ e}^{-} \text{ \AA}^{-2}$. A rebinning factor of m means m^2 pixels of the original SI are combined into one pixel in the new SI. Symbol color represents electron dose used in the STEM-EDX scan.

a typical PSC lamella, n for the bulk perovskite can easily reach 50 000, whereas in high magnification experiments, a small-area scan over ≈ 100 pixels might be desirable to establish the composition of small inclusions or precipitates. Even with an n value as low as 100, the AE would still only be in the range of 2.4–5.4%, 2.5–5.0%, and 2.5–7.0% for Pb- L_{α} , I- L_{α} , and Br- K_{α} respectively, assuming similar σ values. This means that even in highly heterogeneous specimens (many precipitates or segregation of certain elements in particular areas), small volumes of such heterogeneities are sufficient to accurately obtain their compositions.

In practice, this many-pixel approach can be done by performing spatial rebinning. This step transforms (a portion of) the original SI into a new one with fewer pixels by summing data from a few neighboring pixels into one pixel. Spatial rebinning thereby reduces RE and enables a more accurate quantification at the cost of lower spatial resolution (Figure 2c,d, Figure S5, Supporting Information). One may also perform spectral rebinning to a greater extent than the one used in this work (5 to 20 eV per channel) to further reduce RE at the expense of lower spectral resolution. Importantly, rebinning is also a powerful approach to achieve PD without resorting to high doses. For example, spatially rebinning the $400 (1200) \text{ e}^{-} \text{ \AA}^{-2}$ SI by a factor of 3 (2) allows the Br- K_{α} peak to achieve PD (Figure S5, Supporting Information). However, one should not acquire an SI with low dose and very high spatial resolution, with a plan to spatially rebin it later, without first considering beam broadening, possible oversampling, and the consequent compounded beam damage. This is especially true when working on a thick specimen such as the lamella used in this work. In summary, the data displayed in Figure 2 shows that pixel-by-pixel quantification

at 10 nm per pixel spatial resolution suffers from a large error at the dose range examined. However, we can gather data from many pixels in an SI through spatial rebinning to achieve sufficient statistical confidence for quantification of the elements of interest. Depending on the level of precision and resolution desired, one may obtain information from both the original and rebinned SIs. The original SI provides qualitative elemental maps showing compositional heterogeneity at high spatial resolution, while the rebinned SI supplies accurate quantitative compositions for specific areas of interest.

Once the PD of important elemental peaks has been confirmed and measurement errors have been estimated at the desired spatial resolution, the background-corrected intensity data may be converted into quantitative compositional maps using either Cliff-Lorimer or ζ -factor quantification.^[23,24] Importantly, each EDX analysis program/suite may have its own threshold of minimum peak intensity required for quantification. For example, the analysis platform we used, HyperSpy, can not quantify SIs acquired with the 2 lowest doses. Quantitative maps extracted from the remaining 10 SIs are displayed in Figure S6 (Supporting Information).

To obtain a quantitative measure of beam damage, we monitor changes in X/Pb (X = I, Br) STEM-EDX peak intensity ratios and after/before HAADF intensity ratio as the dose is increased. The intensity (I) of a HAADF image is proportional to specimen thickness (t) and its effective atomic number (Z_{eff}) as follows^[21,25]

$$I = tZ_{\text{eff}}^{1.8} \quad (3)$$

Intensity changes can thus be used as a proxy to gauge the extent of mass loss due to vacancy formation and volatilization.

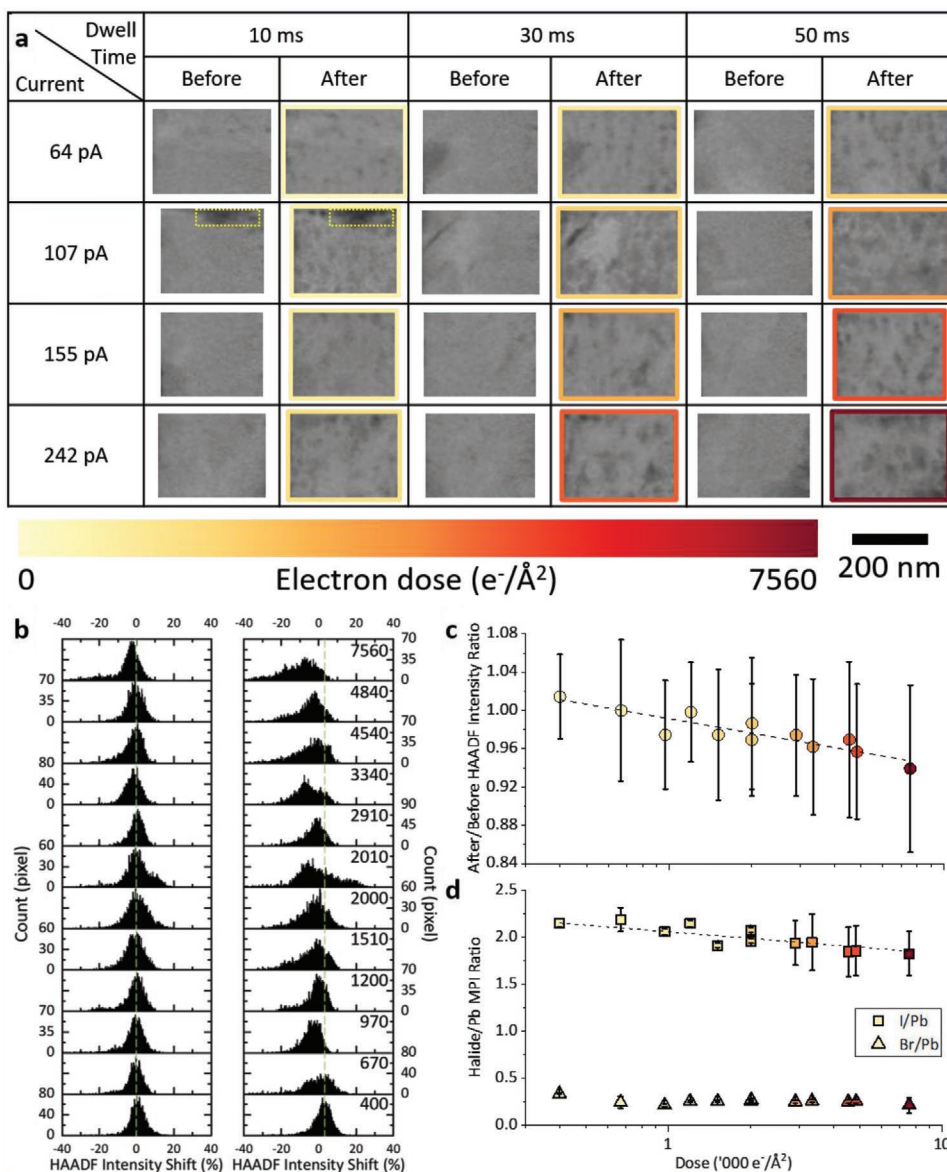


Figure 3. a) HAADF images of the perovskite layer acquired before and after the STEM-EDX scans. Dotted rectangles in the (107 pA, 10 ms) image pair mark an area which is masked in intensity measurement. The imaged areas are of slightly different sizes due to local changes in perovskite layer thickness. b) Intensity histograms and c) after/before intensity ratio plot of the HAADF images shown in panel (a). Green dashed lines in panel b) mark the positions of the $400 \text{ e}^- \text{ \AA}^{-2}$ peaks. d) Halide/Pb MPI ratio plot extracted from the STEM-EDX data. Error bars represent standard deviations across all perovskite pixels in an SI. The ‘After’ image frame color in panel (a) and symbol color in panels (c) and (d) represent electron dose used in the STEM-EDX scan. In panels (c) and (d), dashed lines highlight the exponential decline trend and do not represent measured data.

Comparing the ‘before’ and ‘after’ HAADF images in **Figure 3a**, STEM-EDX clearly affects the perovskite layer. Histograms of HAADF intensity acquired before the STEM-EDX data (**Figure 3b**, left column), show similar distributions for the different areas. As peak heights and full width at half maximum values are comparable, we conclude that the thickness and composition of the lamella are initially uniform. With rising electron doses used for STEM-EDX mapping, the corresponding HAADF intensity distributions broaden, with the maximum gradually shifting toward lower counts for the ‘after’ scans. The peaks also become less symmetrical as the low-intensity tails grow, corresponding to

the larger, darker speckles visible in the images of higher dose STEM-EDX scans (**Figure 3a**). These trends are also captured by taking an after/before average intensity ratio, which declines exponentially as electron dose increases (**Figure 3c**). Although the average intensity only drops by up to 6% for the dose range investigated in this work, the large standard deviations (error bars in **Figure 3c**) indicate that beam damage causes an increase in compositional heterogeneity. This effect is likely related to the perovskite’s inherent nanoscale heterogeneity, such as variation of grain orientation which has been found to affect robustness against beam damage.^[26,27]

Interpreting HAADF intensity using Equation 3, given the composition and thickness of the lamella, a 6% decline could be explained by:

- A 6% loss of the number of TCDH perovskite unit cells in the region under the beam (complete volatilization);
- A 3.4% reduction of Z_{eff} ;
- A combination of the above.

We note that a transformation of TCDH perovskite into PbI_2 without additional and substantial mass loss would result in a brightening of HAADF intensity driven by the large increase in density (see Note S2, Supporting Information). As we do not observe this in our images, we conclude that TCDH perovskite does not decompose to PbI_2 under irradiation at the dose range explored.

The halide/Pb MPI ratios and their standard deviations are shown in Figure 3d. While the Br/Pb ratio stays approximately constant before dropping only at the highest dose, the I/Pb ratio declines exponentially, decreasing by 15% from the lowest dose to the highest. This finding is expected as decomposition studies have shown that bromide ions are more stable compared to iodide.^[28,29] Indeed, electron beam-induced bromine desorption has only been observed in CsPbBr_3 nanocrystals whose dimensions are orders of magnitude lower than a typical PSC lamella.^[12,30] This 15% drop in I/Pb ratio is in very good agreement with the 3.4% reduction in Z_{eff} inferred from the HAADF intensity, which corresponds to a $\approx 16\%$ iodine loss (Note S2 and Figure S7, Supporting Information). This similarity confirms that the main damage mechanism is through formation of iodine vacancies rather than complete evaporation, as the latter would have resulted in no changes to the I/Pb ratio. Iodine vacancies could have been formed through iodine diffusion into the spiro-OMeTAD layer, which is found to occur to a greater extent with increasing dose (Figure S8, Supporting Information).

The exponential decline in both HAADF intensity and I/Pb ratio highlight the necessity of minimizing electron dose, even in the absence of PbI_2 formation. The observed trend suggests radiolysis as the beam damage mechanism as it has been shown to exhibit an exponential dependence on total dose.^[19] Further, it indicates that dose rate has minimum impact on beam damage, as previous works conducted with parallel beam TEM-EDX also observed a similar decline of I/Pb ratio in MAPbI_3 .^[9,10,14] We note that factors other than total dose may affect the extent of radiolysis, such as electron beam energy or sample thickness (or surface/volume ratio).^[13] Here both are nominally constant, so have been disregarded from the analysis. Furthermore, precautionary measures such as carbon coating may be used to reduce beam damage by reducing the loss of volatile species formed during irradiation.^[15,19,31] Note that this would not necessarily preserve crystallographic structure, but just overall composition.

We investigate the relationship between electron dose, quality of STEM-EDX signal, and beam damage for quantitative analysis of a TCDH perovskite as a model beam-sensitive material with a complex chemistry. In particular, we outline five parameters which may be used to quantify STEM-EDX data quality and beam-induced chemical changes: peak detectability, relative measurement error on a pixel-by-pixel-basis, absolute measurement error for multiple pixels, HAADF intensity ratio, and elemental peak intensity ratio. Peak detectability at a spatial resolution of (10/20/30) nm per pixel is achieved for Br- K_{α} , I- L_{α}

and Pb- L_{α} peaks with a dose of (2910/1200/400) $\text{e}^- \text{\AA}^{-2}$. Highly accurate quantification on a pixel-by-pixel basis is not possible at the dose range and spatial resolution used here, but can be done at a lower spatial resolution by gathering data from multiple pixels through spatial rebinning. We then quantify beam damage across an electron dose range of 400–7560 $\text{e}^- \text{\AA}^{-2}$ for a specimen of ≈ 200 nm nominal thickness and observe that both HAADF intensity and I/Pb peak intensity ratios decline exponentially with dose. These declines underline the necessity of minimizing electron dose while maintaining statistical confidence in the characterization results, even though we do not observe decomposition of perovskite into PbI_2 . This delicate balancing act calls for the simultaneous use of advanced hardware and post-processing techniques, such as large-area EDX detectors, spatial and spectral rebinning, and data denoising. This work presents suggestions for acquisition and data analysis that can be extended to compositional studies of other beam-sensitive compounds such as metal-organic frameworks or polymeric materials. A deeper understanding of X-ray generation and collection, as well as judicious application of analysis tools, can improve statistical confidence in future STEM-EDX characterization of delicate materials.

Experimental Section

The TCDH PSC device was fabricated following the method described in ref. [20].

A cross-sectional TEM lamella was prepared with an FEI Helios Nanolab Dualbeam FIB/SEM as detailed in Figure S1 (Supporting Information). This lamella was immediately transferred into an FEI Osiris FEG-(S)TEM, minimizing air exposure to ≈ 2 min. HAADF images were acquired with a Fischione detector, a spatial sampling of 4 nm per pixel and a dwell time of 1 μs . STEM-EDX SIs were obtained with Bruker Super-X SDDs with a total collection solid angle of ≈ 0.9 sr, a spatial sampling of 10 nm per pixel, and a spectral resolution of 5 eV per channel. 12 combinations of electron beam current (64, 107, 155, 242 pA) and dwell time (10, 30, 50 ms) values were used to achieve a series of electron doses, ranging from 400 to 7560 $\text{e}^- \text{\AA}^{-2}$. STEM-EDX SIs were spectrally rebinned to 20 eV per channel, then denoised with PCA and processed in HyperSpy, a Python-based analysis suite for hyperspectral data.^[32]

Supporting Information

Supporting Information is available from the Wiley Online Library or from the author.

Acknowledgements

F.U.K. thanks the Jardine Foundation and Cambridge Trust for a doctoral scholarship. S.C. thanks funding from the European Union's Horizon 2020 research and innovation programme under the Marie Skłodowska-Curie Grant Agreement N845612. The research leading to these results has received funding from the European Union Horizon 2020 Research Infrastructures research and innovation programme under grant agreement No. 823717 - ESTEEM3. The authors thank Dr. Mojtaba Abdi-Jalebi (Cavendish Laboratory, University of Cambridge, now at Institute of Materials Discovery, University College London) for PSC fabrication.

Conflict of Interest

The authors declare no conflict of interest.

Keywords

energy materials, energy-dispersive X-ray spectroscopy, microscopy and imaging methods, perovskite solar cells, transmission electron microscopy

Received: September 7, 2020

Revised: September 25, 2020

Published online:

-
- [1] H. J. Snaith, *Nat. Mater.* **2018**, *17*, 372.
- [2] J.-P. Correa-Baena, M. Saliba, T. Buonassisi, M. Grätzel, A. Abate, W. Tress, A. Hagfeldt, *Science* **2017**, *358*, 739.
- [3] T. A. S. Doherty, A. J. Winchester, S. Macpherson, D. N. Johnstone, V. Pareek, E. M. Tennyson, S. Kosar, F. U. Kosasih, M. Anaya, M. Abdi-Jalebi, Z. Andaji-Garmaroudi, E. L. Wong, J. Madeo, Y.-H. Chiang, J.-S. Park, Y.-K. Jung, C. E. Petoukhoff, G. Divitini, M. K. L. Man, C. Ducati, A. Walsh, P. A. Midgley, K. M. Dani, S. D. Stranks, *Nature* **2020**, *580*, 360.
- [4] J. Hidalgo, A. Castro-Méndez, J. Correa-Baena, *Adv. Energy Mater.* **2019**, *9*, 1900444.
- [5] D. E. Newbury, *Scanning* **2006**, *27*, 227.
- [6] C. M. Parish, L. N. Brewer, *Ultramicroscopy* **2010**, *110*, 134.
- [7] S. Cacovich, F. Matteocci, M. Abdi-Jalebi, S. D. Stranks, A. Di Carlo, C. Ducati, G. Divitini, *ACS Appl. Energy Mater.* **2018**, *1*, 7174.
- [8] N. Klein-Kedem, D. Cahen, G. Hodes, *Acc. Chem. Res.* **2016**, *49*, 347.
- [9] J. Ran, O. O. Dyck, X. Wang, B. Yang, D. B. Geohegan, K. Xiao, *Adv. Energy Mater.* **2020**, *10*, 1903191.
- [10] M. U. Rothmann, W. Li, Y. Zhu, A. Liu, Z. Ku, U. Bach, J. Etheridge, Y.-B. Cheng, *Adv. Mater.* **2018**, *30*, 1800629.
- [11] M. U. Rothmann, W. Li, J. Etheridge, Y.-B. Cheng, *Adv. Energy Mater.* **2017**, *7*, 1700912.
- [12] Z. Dang, J. Shamsi, F. Palazon, M. Imran, Q. A. Akkerman, S. Park, G. Bertoni, M. Prato, R. Brescia, L. Manna, *ACS Nano* **2017**, *11*, 2124.
- [13] S. Chen, Y. Zhang, J. Zhao, Z. Mi, J. Zhang, J. Cao, J. Feng, G. Zhang, J. Qi, J. Li, P. Gao, *Sci. Bull.* **2020**, *65*, 1643.
- [14] S. Chen, X. Zhang, J. Zhao, Y. Zhang, G. Kong, Q. Li, N. Li, Y. Yu, N. Xu, J. Zhang, K. Liu, Q. Zhao, J. Cao, J. Feng, X. Li, J. Qi, D. Yu, J. Li, P. Gao, *Nat. Commun.* **2018**, *9*, 4807.
- [15] S. Chen, Y. Zhang, X. Zhang, J. Zhao, Z. Zhao, X. Su, Z. Hua, J. Zhang, J. Cao, J. Feng, X. Wang, X. Li, J. Qi, J. Li, P. Gao, *Adv. Mater.* **2020**, *32*, 2001107.
- [16] C. Eames, J. M. Frost, P. R. F. Barnes, B. C. O'Regan, A. Walsh, M. S. Islam, *Nat. Commun.* **2015**, *6*, 7497.
- [17] J. M. Azpiroz, E. Mosconi, J. Bisquert, F. De Angelis, *Energy Environ. Sci.* **2015**, *8*, 2118.
- [18] J. Haruyama, K. Sodeyama, L. Han, Y. Tateyama, *J. Am. Chem. Soc.* **2015**, *137*, 10048.
- [19] R. F. Egerton, *Micron* **2019**, *119*, 72.
- [20] M. Abdi-Jalebi, Z. Andaji-Garmaroudi, S. Cacovich, C. Stavrakas, B. Philippe, J. M. Richter, M. Alsari, E. P. Booker, E. M. Hutter, A. J. Pearson, S. Lilliu, T. J. Savenije, H. Rensmo, G. Divitini, C. Ducati, R. H. Friend, S. D. Stranks, *Nature* **2018**, *555*, 497.
- [21] D. B. Williams, C. B. Carter, *The Transmission Electron Microscope*, Springer, New York **1996**.
- [22] H. A. Liebhafsky, H. G. Pfeiffer, E. H. Winslow, P. D. Zerny, *X-Rays, Electrons and Analytical Chemistry*, John Wiley & Sons, New York **1972**.
- [23] G. Cliff, G. W. Lorimer, *J. Microsc.* **1975**, *103*, 203.
- [24] M. Watanabe, D. B. Williams, *J. Microsc.* **2006**, *221*, 89.
- [25] P. Hartel, H. Rose, C. Dinges, *Ultramicroscopy* **1996**, *63*, 93.
- [26] E. M. Tennyson, T. A. S. Doherty, S. D. Stranks, *Nat. Rev. Mater.* **2019**, *4*, 573.
- [27] S. Chen, P. Gao, *J. Appl. Phys.* **2020**, *128*, 010901.
- [28] J. Yang, X. Liu, Y. Zhang, X. Zheng, X. He, H. Wang, F. Yue, S. Braun, J. Chen, J. Xu, Y. Li, Y. Jin, J. Tang, C. Duan, M. Fahlman, Q. Bao, *Nano Energy* **2018**, *54*, 218.
- [29] W. Tan, A. R. Bowring, A. C. Meng, M. D. McGehee, P. C. McIntyre, *ACS Appl. Mater. Interfaces* **2018**, *10*, 5485.
- [30] Z. Dang, J. Shamsi, Q. A. Akkerman, M. Imran, G. Bertoni, R. Brescia, L. Manna, *ACS Omega* **2017**, *2*, 5660.
- [31] R. F. Egerton, P. Li, M. Malac, *Micron* **2004**, *35*, 399.
- [32] F. de la Peña, V. T. Fauske, P. Burdet, E. Prestat, P. Jokubauskas, M. Nord, T. Ostasevicius, K. E. MacArthur, M. Sarahan, D. N. Johnstone, J. Taillon, A. Eljarrat, V. Migunov, J. Caron, T. Furnival, S. Mazzucco, T. Aarholt, M. Walls, T. Slater, F. Winkler, B. Martineau, G. Donval, R. McLeod, E. R. Hoglund, I. Alxneit, I. Hjorth, T. Henninen, L. F. Zagonel, A. Garmannslund, A. Skorikov, **2018**, <https://doi.org/10.5281/zenodo.1469364>